Hopping behavior in the Kuramoto–Sivashinsky equation

Peter Blomgren,[a)] Scott Gasner,[b)] and Antonio Palacios[c)]
Nonlinear Dynamical Systems Group, Department of Mathematics & Statistics, San Diego State University, San Diego, California 92182

We report the first observations of numerical "hopping" cellular flame patterns found in computer simulations of the Kuramoto–Sivashinsky equation. Hopping states are characterized by nonuniform rotations of a ring of cells, in which individual cells make abrupt changes in their angular positions while they rotate around the ring. Until now, these states have been observed only in experiments but not in truly two-dimensional computer simulations. A modal decomposition analysis of the simulated patterns, via the proper orthogonal decomposition, reveals spatio-temporal behavior in which the overall temporal dynamics is similar to that of equivalent experimental states but the spatial dynamics exhibits a few more features that are not seen in the experiments. Similarities in the temporal behavior and subtle differences in the spatial dynamics between numerical hopping states and their experimental counterparts are discussed in more detail. © *2005 American Institute of Physics*. [DOI: 10.1063/1.1848311]

Previous experimental works have revealed that the spatio-temporal dynamics of pre-mixed flames exhibit a wide variety of cellular patterns that can change in space and time. Aided by a new numerical scheme, we have found a particular dynamic pattern, called hopping state, through the integration of the Kuramoto–Shivashinsky flame instability model. In this work, we employ the proper orthogonal decomposition to unravel the spatio-temporal characteristics of the numeric hopping states and compare their spatial and temporal features with those obtained in laboratory experiments.

I. INTRODUCTION

Premixed gases burn irregularly, which can lead to cellular flame patterns[7] formed through a mechanism that resembles that of reaction-diffusion systems described first by Turing.[2] When the gases are confined to circular domains, the cells generically become organized in stationary and nonstationary concentric rings. Stationary patterns are steady states with petal-like structures and well-defined spatial symmetries. Nonstationary patterns are dynamical states that change continuously in space and time. The cells move either individually or collectively within the ring structure. The global dynamics could be as simple as a uniformly rotating cell or more complicated as an aggregation of cells moving chaotically.[3] An individual pattern, either stationary or nonstationary, is selected based on control parameters such as type of fuel, pressure, flow rate, and fuel-to-oxidizer ratio.

In previous work,[4] we analyzed the behavior of certain dynamic patterns, called "hopping" states,[1,5] in which individual cells sequentially make abrupt changes in their angular positions while they keep rotating in a ring structure. We

considered isolated rings of hopping states as well as concentric rings of cells in which the outer ring remains stationary while the inner ring exhibits hopping motion. The analysis was based solely on experimental data and the use of the proper orthogonal decomposition (POD). A comparative analysis against computer-simulated hopping states was precluded by the lack of a reliable model of the combustion of premixed gases that can produce solutions with truly two-dimensional features similar to those observed in experiments.[6] There have been, however, reports of similar states, described as "Pushme-Pullyou," found in a quasi-one-dimensional thermodiffusive model.[7] But now, aided by a new numerical DAF-based scheme that we describe in a companion paper,[8] we have observed for the first time a truly two-dimensional (2D) hopping state. The state was found in simulations of the Kuramoto–Sivashinsky (KS) model,[9,10] which is considered to be one of the simplest models of thermodiffusive instability and one that can produce solutions that closely resemble experimental states, including stationary and dynamic patterns. The actual hopping state is a single-ring state made up of three cells and it was found in a very small region of parameter space bounded by two stationary patterns, one with three cells and one with four. A POD analysis reveals the emergence of a spatio-temporal pattern whose temporal characteristics are in good agreement, up to a few subtle differences in spatial behavior, with those of experimental states. More importantly, we show that the POD analysis suggests that numerical hopping patterns are created in an invariant subspace where three steady-state modes compete for stability. The spatial symmetries of these modes are described by the Dihedral groups $\mathbf{D}_3$, $\mathbf{D}_2$, and $\mathbf{D}_4$. With this information, we can derive appropriate normal forms equivariant under $\Gamma = \mathbf{O}(\mathbf{2})$, the group of rotations and reflections of the experiments, and then use the normal forms to study hopping-modulated rotating states and hopping–rotating state transitions and interactions. This task is part of future work.

a)Electronic mail: blomgren@terminus.sdsu.edu
b)Electronic mail: sgasner@yahoo.com
c)Electronic mail: palacios@euler.sdsu.edu

15, 013706-1

The paper is organized as follows. In Sec. II we discuss the experimental work in more detail. In Sec. III we describe the Kuramoto–Sivashinky model, carry out a linear stability analysis, and review the basic principles and properties of the proper orthogonal decomposition relevant to this work. In Sec. IV we derive the marginal stability curves that guided us in the search for hopping states; we show results of the numerical integration of the KS model with the new DAF-based technique; and present a complete bifurcation analysis, via the POD technique, of the observed spatio-temporal dynamics. Similarities in the temporal behavior and subtle differences in the spatial dynamics between numerical hopping states and their experimental counterparts are discussed in this section as well.

II. COMBUSTION EXPERIMENTS

A. Experimental setup

Experiments with pre-mixed gases on a circular porous plug burner were conducted at the University of Houston by collaborator M. Gorman.[1] The burner was mounted inside a combustion chamber and pressure was kept within the range 0.3–0.5 atm. Fuel and air were mixed prior to their entrance into the porous medium. Pressure, flow rate, and fuel/oxidizer ratio were controlled to within 0.1%. Depending on initial conditions, a steady uniform flame in the form of a circular luminous disk, 5.62 cm in diameter and 0.5 mm thick, appears roughly 5 mm above the surface of the burner. We call this initial state the "trivial solution" or "uniform state" of the experiment. To the experimentalist, the trivial solution looks the same if the burner is rotated by an arbitrary angle, or if the experiment is observed through a vertical mirror. It is then reasonable to identify the orthogonal group $\mathbf{O(2)}$, i.e., the group of rotations and reflections on the plane, as the underlying group of symmetries of the flame experiments. Upon changes of principal parameters, the trivial solution loses stability and then ordered patterns of concentric rings of cells emerge via $\mathbf{O(2)}$ symmetry-breaking bifurcations. In a typical experiment, different patterns are selected by varying the flow rate and the equivalence ratio. Variations in the pressure are made to adjust the range of the number of cells. For example, single rings of cells are stable at 0.3 atm, but not at 0.5 atm. Changing the fuel can lead to additional patterns; ratcheting states, for instance, are found in isobutane–air mixtures but not in propane–air mixtures.[1]

Brighter cells correspond to hotter regions on the burner. They are separated by darker regions corresponding to cusps and folds which extend an additional 5 mm away from the surface of the burner. Emergent patterns include a wide variety of steady state ordered patterns and dynamical states in which the cells are able to move orderly within a ring configuration or chaotically.[11] Steady states can be classified based on their spatial symmetries—usually, a subgroup of $\mathbf{O(2)}$ would suffice for single-ring patterns while direct products of subgroups might be necessary for multiple rings. In contrast, dynamical states would require a combination of
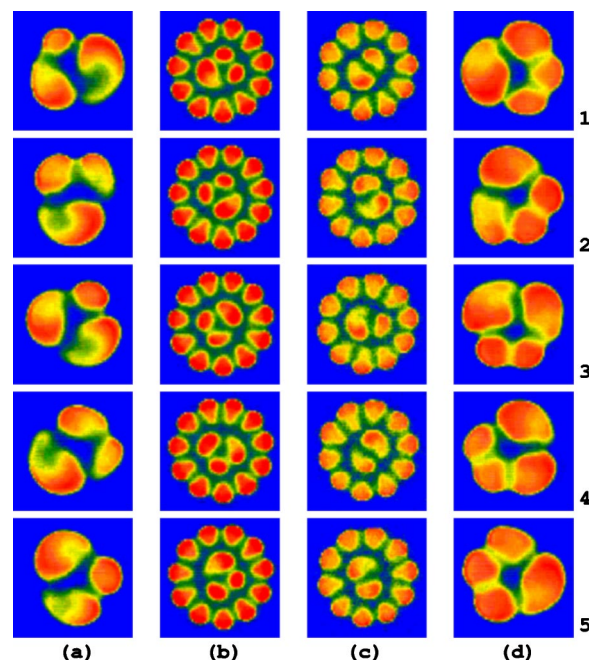

FIG. 1. Four sequential frames of videotape of four different experimental states with hopping motion in: (a) A single ring state with three cells; (b) an inner ring of three cells surrounded by a stationary outer ring with eleven cells; (c) an inner ring of two cells surrounded by a stationary outer ring with ten cells; (d) a single ring state with four cells.

spatial and temporal symmetries. Of particular interest to this work are a special type of nonuniformly traveling wave patterns, called "hopping states," in which individual cells sequentially make abrupt changes in their angular positions. These type of dynamic states appear in either single-ring or multiple-ring configurations. And they have been observed only in isobutane–air flames but not in propane–air flames. Figure 1 depicts four different configurations of hopping states. In Figs. 1(a) and 1(d), hopping occurs in a single ring array of cells, while in Figs. 1(b) and 1(c), an inner ring of hopping cells is surrounded by a stationary outer ring.

Cells in hopping states evolve collectively like rotating waves, yet individually, their motion appears more complicated and very different from other types of traveling wave patterns found in experiments.[12] For instance, hopping cells do not rotate rigidly. Each cell seems to hop independently while still preserving the overall dynamics of the ring. That is, there is a timingly rhythm for each cell to move faster and to slow down. Closer observation also reveals that when a cell is hopping, its shape is more asymmetric than the other cells which appear temporarily stationary.

B. Experimental measurements

Video images of relevant flame experiments were collected with a Dage-MTI Charge-Coupled Device camera mounted vertically on top of the experimental system. The video images capture the emitted chemiluminescence from the flame front and provide a two-dimensional measurement proportional to the temperature at various points on the burner. Such measurements are commonly used in flame models.[10,13] The spatial and temporal resolution, the time

interval, and the dynamic range are limited only by the recording device. Images of 640×480 pixel resolution, taken at $1/30$ second intervals with 7 bit dynamic range, are typical for dynamics recorded on S-VHS video tape.

III. MODEL OF FLAME INSTABILITY

A. The Kuramoto–Sivashinsky equation

Motivated by a new numerical DAF-based scheme that we have recently developed and described in Ref. 8, we now explore in this work the formation and evolution of hopping states through a modified version of the Kuramoto–Sivashinky equation

$$\frac{\partial u}{\partial t} = \varepsilon u - (1 + \nabla^2)^2 u - \eta_1 (\nabla u)^2 - \eta_2 u^3, \qquad (1)$$

where $u = u(\mathbf{x}, t)$ represents the perturbation of a planar flame front in the direction of propagation, ε measures the strength of the perturbation force, η_1 is a parameter associated with growth in the direction normal to the burner, and $\eta_2 u^3$ is a term that was added to help stabilize the numerical integration. This model is derived by making a series of simplifying assumptions on a pair of diffusion equations [for a single chemical species and temperature $u(\mathbf{x}, t)$] coupled to fluid equations. We have chosen this model because it is one of the simplest models of the thermodiffusive instability[9,10] and because through previous work[14] we have established that the DAF-based numerical scheme can produce accurate simulations of various experimental flame patterns. Additionally, we have validated the accuracy of the KS model and of the DAF technique by comparison with simulations of the Brusselator equations, which were carried out in previous work using an alternating direction implicit (ADI) numerical scheme.[12] Both schemes, DAF and ADI, produce qualitatively similar results, except that the ADI rapidly develops a divergence near the origin of a polar grid. Our aim is now to use the numerical simulations to get insight into the underlying bifurcations that lead to hopping states. We treat the radius of the burner as the distinguished bifurcation parameter, while the other parameters are held fixed. In order to conduct simulations that are relevant to the experiments, i.e., simulations that preserve the $\mathbf{O(2)}$ symmetry of the burner, we integrate (1) in a circular domain of radius R through polar coordinates $\mathbf{x} = (r, \theta)$ and Dirichlet boundary conditions $u(\mathbf{x}, t) = 0$ outside of this domain. In the next section we present a brief description of the DAF-based integration scheme. More in-depth details of the actual numerical algorithm can be found in Ref. 8.

B. Second-generation DAF integration scheme: Basic ideas

Efforts to numerically investigate Gorman's flames with the KS equation (1) had been unsuccessful due to a singularity that arises in the Laplacian operator $\nabla^2 = (\partial_{rr} + 2r^{-1}\partial_r + r^{-2}\partial_{\phi\phi})$ near the origin of a polar grid (circular burner). Even though the singularity can be avoided by partitioning each diameter into an even number of equally spaced lattice points, the presence of small denominators at grid points close to the origin necessitates very accurate estimates of

spatial derivatives. To solve this problem, we originally developed an algorithm[14] that uses "distributed approximating functionals"[15–17] to approximate the flame front $u(x, t)$ and its derivatives with a specified accuracy on and off grid points close to the origin as follows. A distributed approximating functional (DAF) is an approximation of identity in the weak sense:

$$(-1)^n f^{(n)}(x) = \int_{-\infty}^{\infty} \delta^{(n)}(x) f(x) dx \to (-1)^n f^{(n)}(x)$$

$$\approx \int_{-\infty}^{\infty} \delta_{\mathrm{DAF}}^{(n)}(x) f(x) dx. \qquad (2)$$

Robust DAFs are built by multiplying a Gaussian by a finite sum of Hermite polynomials,[15]

$$\delta_{\mathrm{DAF}}(x) = \frac{1}{\sqrt{2\pi}\sigma} e^{(-x^2/2/\sigma^2)} \times \sum_{n=0}^{M/2} \left(\frac{-1}{4}\right)^n \frac{1}{n!} H_{2n}\left(\frac{x}{\sqrt{2}\sigma}\right), \qquad (3)$$

where M is the order of approximation, and σ an appropriate decay-rate for the exponential. DAFs are particularly well-suited for approximating spatial derivatives on nonuniform grids since the error bound for the approximation is uniform over the entire domain, even off the node points. The DAF-based time-integration scheme for the KS model can be written in the form

$$\frac{u(t+h) - u(t)}{h} = F\left(x, t + \frac{h}{2}, \frac{u(t+h) + u(t)}{2}\right),$$

where $F(\cdot)$ is the right-hand-side of (1); the nonlinear terms in F are then *linearized* by the following first-order approximation:

$$\left[\frac{u(t+h) + u(t)}{2}\right]^n \approx \left(1 - \frac{n}{2}\right) u(t)^n + \frac{n}{2} u(t)^{n-1} u(t)(t+h).$$

Shortly after the scheme was completed, we observed for the first time several stationary cellular flame patterns with multiple rings and a few dynamic states such as single rings of rotating cells, see Ref. 15 for more details. More complicated dynamic states were also observed but only for brief periods of time. The resulting scheme was linear, and consequently, unstable for integration over long periods of time, which are typically required for simulating highly complex patterns. But recently,[14] we have developed a second-generation code with a new stable DAF-based time-integration algorithm, based on a Crank–Nicolson scheme

$$\frac{u(t+h) - u(t)}{h} = \frac{F(x, t, u(t)) + F(x, t+h, u(t+h))}{2}. \qquad (4)$$

Advantages of this new algorithm are: (i) Unconditional stability,[18] and (ii) time-discretization becomes second order. We remark that the Crank–Nicolson (CN) scheme is used only for the discretization in time. Furthermore, by keeping the full nonlinearity of $F(\cdot)$, the spatial approximation retains the order of the DAF-approximation. Once the DAF-approximation is used for the spatial derivatives in (4), the resulting nonlinear system of equations is solved for the un-
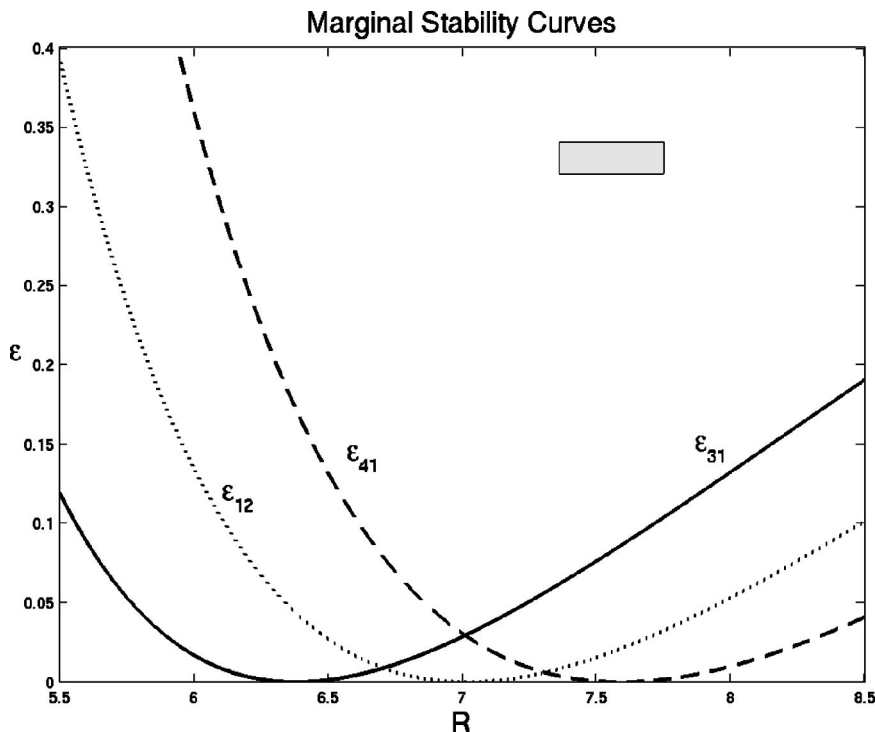
FIG. 2. Marginal stability curves outline the stability domains where the trivial solution $u_0=0$ (representing a uniform flame front) bifurcates to Fourier–Bessel modes Ψ_{nm}.

known $\vec{u}(\vec{x},t+h)$. We formulate this step as a root finding problem $\vec{G}(\vec{u}(\vec{x},t+h))=0$, which we solve using an iterative Newton-based method:

$$\vec{u}^{n+1}(\vec{x},t+h) = \vec{u}^n(\vec{x},t+h) - [\,\delta\vec{G}(\vec{u}^n(\vec{x},t+h))\,]^{-1}\vec{G}(\vec{u}^n(\vec{x},t+h)),$$

$$\vec{u}^0(\vec{x},t+h) = \vec{u}(\vec{x},t),$$

where $\delta\vec{G}$ is the Jacobian $\delta\vec{G}(\vec{u}^n(\vec{x},t+h))=[G_1(\vec{u}^n(\vec{x},t+h))^T,\ldots,G_k(\vec{u}^n(\vec{x},t+h))^T]^T$, and k is the number of grid-points.

C. Stability analysis

To guide us in the search for hopping states, we perform a linear stability analysis as follows. First, we assume $u_0=0$ to be the uniform state or homogenous flame front that is commonly observed in the experiments. Then we investigate the stability of this uniform state to small perturbations of the form:

$$w(r,\theta,t) = e^{\lambda t}\Psi_{nm}(r,\theta) + c.c., \tag{5}$$

where $\Psi_{nm}(r,\theta)=J_n(\alpha_{nm}r/R)e^{in\theta}$ $(m\geq 0$ and $n>0)$ and $J_n(r)$ is the nth order Bessel function of the first kind and α_{nm} is its mth nontrivial zero, and c.c. denotes complex conjugate terms, which render $w(r,\theta,t)$ a real-valued solution. It follows that the uniform flame front is stable if $\lambda<0$, and unstable if $\lambda>0$. In physical space, $\Psi_{nm}(r,\theta)$ has the appearance of a cellular pattern with n cells whose orientation is determined by m. Thus a perturbation based on Fourier–Bessel functions is a natural choice.[12] Now substituting (5) into (1) and using the fact that $\nabla^2\Psi_{nm}+k^2\Psi_{nm}=0$, and $\nabla^4\Psi_{nm}-k^4\Psi_{nm}=0$, where $k^2=(\alpha_{nm}/R)^2$, we arrive at $(\varepsilon-1$

$+2k^2-k^4-\lambda)w=0$. Since we are looking for nontrivial solutions for w, then λ is determined by the roots of characteristic polynomial $\varepsilon-1+2k^2-k^4-\lambda=0$. Hence a marginal stability curve, which corresponds to those parameters where $\lambda=0$, is given (as a function of the radius of the burner) by

$$\varepsilon_{nm}(R) = 1 - 2\left(\frac{\alpha_{nm}}{R}\right)^2 + \left(\frac{\alpha_{nm}}{R}\right)^4. \tag{6}$$

A critical observation is the fact that beyond this curve, on increasing ε, the uniform state $u_0=0$ destabilizes to $\Psi_{nm}(r,\theta)$. More importantly, we now have a tool to systematically search for the right type of pattern, at least with the right number of cells. Similar marginal stability curves were derived to aid the numerical explorations of cellular patterns in a phenomenological model.[4,12,19]

IV. SIMILARITIES AND DIFFERENCES IN SPATIO-TEMPORAL DYNAMICS

Without loss of generality, we choose to focus the integration of the model equation (1) in a region where the evolution of a single-ring pattern with three cells can be traced. Such regions can be found in a neighborhood of the minimum of the marginal stability curve ε_{31} shown in Fig. 2. As the curved is crossed, on increasing R, a stationary pattern of three cells with purely spatial D_3-symmetry emerges via a symmetry-breaking bifurcation from the **O(2)**-invariant trivial solution.

Increasing R further, and upon crossing the left edge of the shaded region, the three-cells pattern loses stability, the
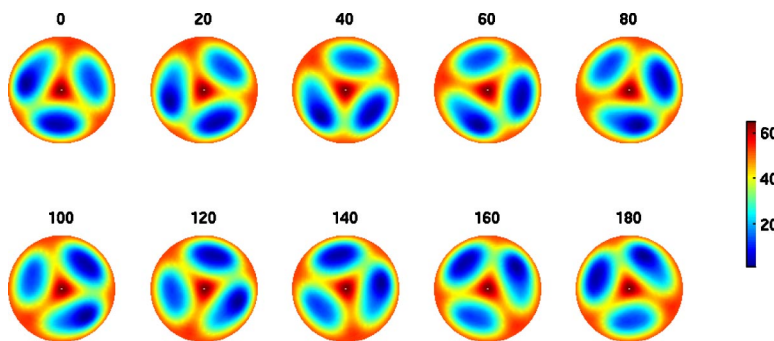
FIG. 3. Ten sequential time (top index) snapshots of a dynamic state of three cells rotating counter-clockwise, with small modulations, found in simulations of (1). Parameter values are: $\varepsilon = 0.32$, $\eta_1 = 1.0$, $\eta_2 = 0.013$, and $R = 7.36$.

D_3-symmetry of the ring is broken, and a dynamic pattern of three cells rotating "almost" uniformly and counter-clockwise bifurcates subcritically. Figure 3 depicts a sample of snapshots of the space and time evolution of the $u(r, \theta, t)$ field obtained at $R = 7.36$. Although at first glance the cells appear to be rotating uniformly and rigidly, i.e., without changing shape, the POD analysis that follows will help us determine in more detail the exact spatio-temporal characteristics of the dynamics.

An ensemble of 2000 consecutive snapshots was generated for the POD analysis. Figure 4 shows the time-average (can be considered mode Φ_0) followed by the ten modes, $\Phi_1 - \Phi_{10}$, with the highest POD energy (see the Appendix for an exact definition). The actual amount of energy in each mode is indicated below each graph. Each mode shows some amount of symmetry. The symmetry of the time-average, in particular, reflects the **O(2)**-symmetry of the burner, even though none of the instantaneous snapshots has this symmetry. This feature is studied in more detail in Ref. 20. The remaining ten modes exhibit, approximately, the following symmetries: Φ_1 and Φ_2 have D_3-symmetry, meaning that one third of a revolution leaves them unchanged; Φ_3 and Φ_4 show D_1-symmetry, i.e., the patterns are restored after one complete revolution; Φ_5 and Φ_6 exhibit D_6-symmetry, which is just a higher harmonic of the first two modes Φ_1 and Φ_2; Φ_7 and Φ_8 are D_2-symmetric; and Φ_9 and Φ_{10} are D_4-symmetric. Observe also that the energy is almost equally distributed between consecutive pairs of modes, indicating the existence of *coupling* pairs or *invariant* subspaces for reconstructing the dynamics: $V_3 = span\{\Phi_1, \Phi_2\}$,

$V_1 = span\{\Phi_3, \Phi_4\}$, $V_6 = span\{\Phi_5, \Phi_6\}$, $V_2 = span\{\Phi_7, \Phi_8\}$, and $V_4 = span\{\Phi_9, \Phi_{10}\}$, where the index n in V_n indicates D_n-symmetry.

The fact that five pairs of modes are needed to capture about 95% of the energy is in clear contrast to the energy distribution of certain uniformly rotating cells that we studied through simulations of a phenomenological model and simulations of the KS model as well.[12,19] Such uniformly rotating cells were also created via steady-state mode interaction but only two pairs of modes were needed to capture almost 100% of the energy. Another significant difference is the fact the Dihedral group of symmetries of the invariant subspaces found in the decomposition of the uniformly rotating cells are in a 1:2 ratio. These assertions suggest that the cells of the state shown in Fig. 3 do not rotate uniformly and that they are created via a steady-state mode interaction through the spaces $V_3 \oplus V_1 \oplus V_6 \oplus V_2 \oplus V_2$. Phase-space projections and relative phase angles shown in Fig. 5 further confirm that the pattern rotates nonuniformly. The temporal modulations are visible in the graph of a_7 vs a_8 and in the associated relative phase angles that appears just below it. Clearly the modulations are very small but this is the case because the pattern is very close to its bifurcation point, i.e., it appears just slightly to the right of $R = 7.36$. Recall that to the left of $R = 7.36$ the three cell state becomes stationary.

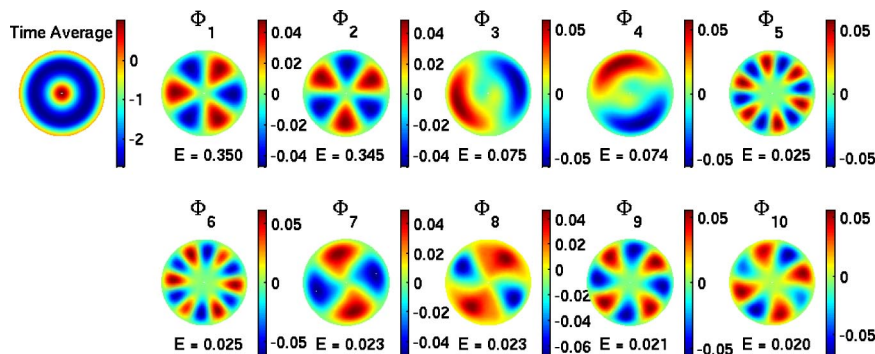Computer animations of the reconstructed dynamics through

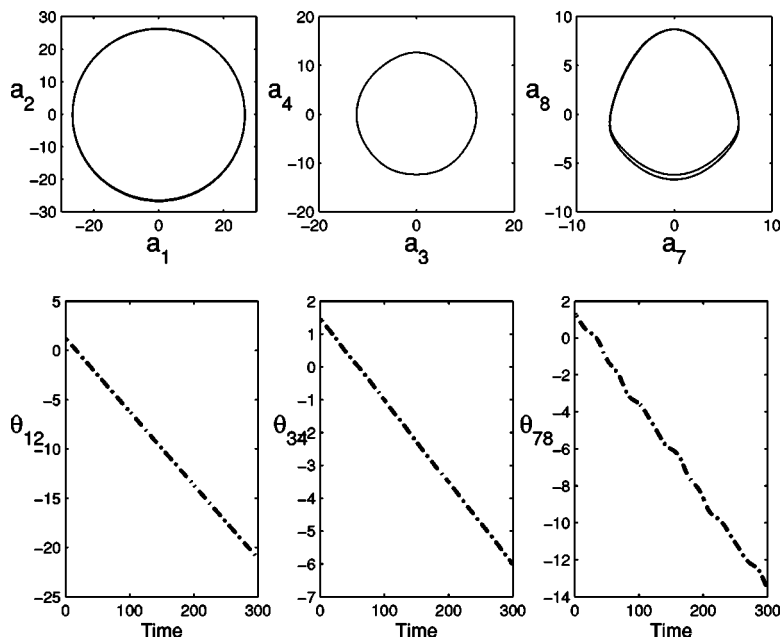FIG. 4. POD decomposition of the three-cells dynamic state of Fig. 3.

FIG. 5. (Top) Phase-space projections produced by the time coefficients of the POD decomposition of the rotating pattern shown in Fig. 3; (bottom) associated relative phase angles.

$$u(\mathbf{x},t) = \tilde{u} + \sum_{k=1}^{M} a_k(t)\Phi_k(\mathbf{x}), \tag{7}$$

show the following features. With $M=2$ modes, a dynamic state emerges with three cells rotating counter-clockwise and almost rigidly (under the naked eye). The asymmetry on each individual cell is almost indistinguishable, but we know from previous work[20,21] that rotating cells cannot posses reflectional (also called "chiral") symmetry. The argument is straightforward. If a solution (cellular state) of a system of differential equations has certain symmetries at one instant of time, then that solution must have the same symmetries at all times. Consequently, any cellular state with reflectional symmetry cannot rotate. With $M=4$ cells, however, the asymmetry in the cells becomes more visible. The cells do not seem to change shape too much, but rather, it is their size that periodically increases and then decreases as the cells rotate. With $M=6$, the cells behave in a similar manner except that their size increases moderately. With $M=8$, the asymmetry in the cells is more pronounced as well as the variations in shape. Also the cells move more independently with small "jumps" in angular position. With $M=10$, the jumps are more visible and the overall temporal motion shows similar characteristics to those of experimental hopping states.[4,5] This last assertion is not a big surprise given the fact that in a POD decomposition of experimental hopping states[4] we found similar modes to those shown in Fig. 4. In particular, we found Φ_1, Φ_2, Φ_7, Φ_8, Φ_9, and Φ_{10}, to be the most dominant modes. It is a surprise, however, that Φ_3–Φ_6 do not appear in the experimental states, not even at lower energy levels. To understand this subtle difference, we performed a numerical experiment of reconstructing the dynamics without Φ_3, Φ_4, and Φ_5. Interestingly, now the reconstructed dynamics resembles more of the hopping motion that is typically observed in the experiments. This better-fit can be

attributed to the fact that now the spatial dynamics is stripped from the oscillations in cell size (without changing shape) that we previously observed in the reconstructions with $M=4$ and $M=6$. Consequently, the periodic "hops" in angular position are more distinguishable.

We now return our attention to the marginal stability curves. On moving right into the shaded region, the modulations on the three-cells state of Fig. 3 become progressively stronger. Near $R=7.74$, in particular, the cells repeatedly make abrupt changes in their angular position while they rotate around the ring; in a manner that more closely resembles experimental observations of hopping cells.[1,5] Figure 6 depicts a few representative snapshots of the spatio-temporal dynamics at $R=7.7475$. Observe that changes in cell shape are more noticeable. In fact, a hopping cell changes its shape more than the other two and also appears more asymmetric. The hops are small in comparison with experimental states but, up to a time-scale factor, the overall characteristics of the dynamics appear to be in good agreement with experiments. To confirm these observations, we perform next a POD analysis of the space-time behavior.

An ensemble of 6000 consecutive snapshots was generated for the POD decomposition. Figure 7 shows the time-average, principal modes, and POD energy, in the same format as they appeared in Fig. 4. A direct comparison of the modes yields the following observations. The invariant sub-spaces V_3, V_2, and V_4 are present in both cases. Modes Φ_3, Φ_4, and Φ_5, in Fig. 7, do not appear in Fig. 4. Mode Φ_{10} in Fig. 7 corresponds to mode Φ_{11} in Fig. 4, though this mode is not shown in Fig. 4. Modes Φ_3 and Φ_4 in Fig. 7 can be thought of being a linear superposition of two concentric modes with D_1-symmetry. In this sense, they are similar to the same modes Φ_3 and Φ_4 of Fig. 4.

Computer animations of the reconstructed dynamics through Eq. (7) shows the following features. With $M=2$
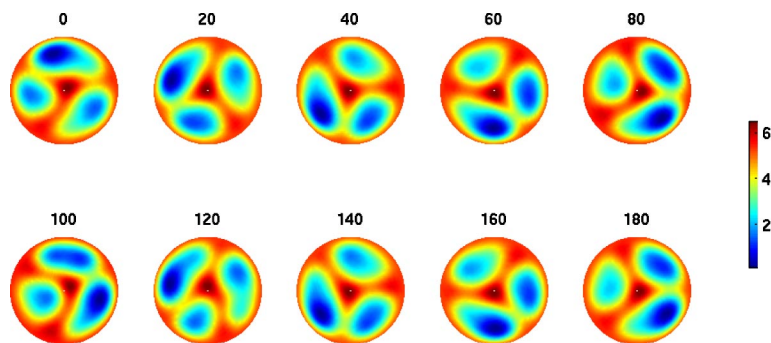
FIG. 6. Space and time evolution of a three-cells hopping state found in simulations of (1). The cells move nonuniformly and their shapes change periodically. Parameter values are: $\varepsilon = 0.32$, $\eta_1 = 1.0$, $\eta_2 = 0.013$, and $R = 7.7475$.

modes, a three-cell dynamic pattern emerges, the cells rotate counter-clockwise and their size and shape is relatively constant at all times. With $M = 4$ modes, the cells now periodically change shape, each cell takes turns changing size, increasing as it moves closer to the edge of the simulated burner and decreasing as it moves toward the center of the burner. This behavior supports the interpretation of Φ_3 and Φ_4 as being made up of two concentric modes with D_1-symmetry. With $M = 5$ modes, the excursions toward the center and boundary of the burner are more noticeable. The smallest cell is always the one pulled towards the center of the burner, just before the leading cell makes an abrupt hop towards the cell behind it. This pulling effect occurs everywhere around the center of the burner, which explains the apparent loss in structure in the fifth mode. With $M = 7$ the cells look more asymmetric with larger changes in shape. With $M = 9$ modes, each cell periodically makes abrupt changes of angular position, jumping closer to the cell immediately in front. This type of hopping motion is clearly more noticeable as compared to the small jumps seen in the previous dynamic state of Fig. 3.

The thickness in the phase-space projections of the POD time coefficients, see Fig. 8, confirms the presence of stronger temporal modulations as compared to those seen in Fig. 5. Stronger modulations explain why the "hopping" motion is now more noticeable. Computer animations of the numerical results will be posted online at http://terminus.sdsu.edu/.

Hence, except for the periodic excursions between the center and boundary of the burner, the spatio-temporal features described by the dynamic state of Fig. 6 are in good agreement with experimental observations of hopping motion.[4,5] The excursions are governed by modes Φ_3, Φ_4, and Φ_5 of Fig. 7. Removing these modes (and Φ_{10} to make the comparison relevant to the states shown in Fig. 1) we observe a dynamic state with spatio-temporal characteristics strongly similar to those seen in Fig. 1, especially in Fig. 1(a).

V. CONCLUSION

We have reported the first observations of "hopping" cellular flame patterns, discovered in numerical simulations of the Kuramoto–Sivashinsky equation through a modified DAF-based integration scheme. Hopping states are characterized by nonuniform rotations of a ring of cells, in which individual cells make abrupt changes in their angular positions while they rotate around a ring. The hopping states that we found exhibit the same temporal features of the experiments but they also show additional spatial features. In particular, a periodic change in the size of the cells followed by periodic excursions between the center and boundary of the simulated burner. A POD analysis of computer simulations reveals the presence of several modes that are similar to those found in experiments, but it also shows the existence of a few other modes that are responsible for the added spatial dynamics. Furthermore, the POD analysis suggests that the numerical hopping states are created through a steady-state mode interaction between three modes whose spatial symmetries are described by the Dihedral groups D_3, D_2, and D_4, respectively. A derivation and analysis of normal form equa-
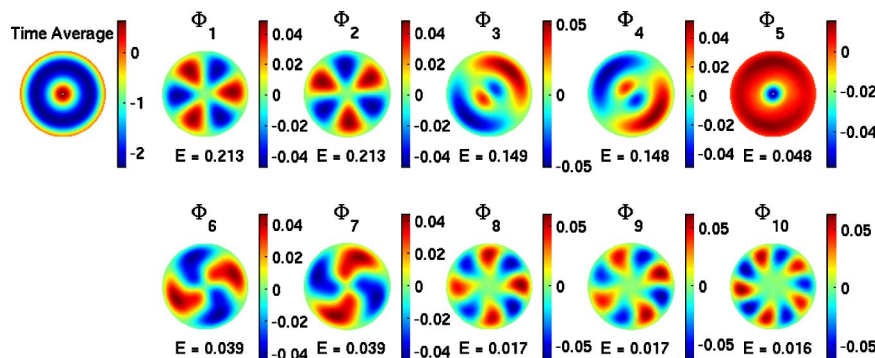

FIG. 7. POD decomposition of the three-cell dynamic state depicted in Fig. 6.
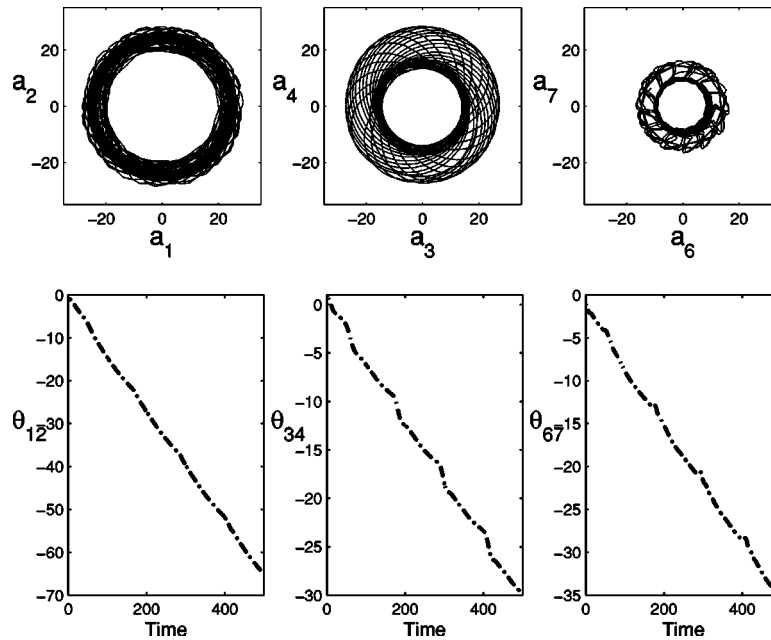
FIG. 8. (Top) Phase-space projections produced by the time coefficients ofnthe POD decomposition of the rotating pattern shown in Fig. 6; (bottom) associated relative phase angles.

tions invariant under the action of these three groups will provide the opportunity to study in more detail the bifurcations of hopping–modulated rotating states and hopping–rotating state transitions and interactions. This task is planned for future work together with a group decomposition[22] of the numerical hopping states.

ACKNOWLEDGMENTS

APPENDIX: MODAL DECOMPOSITION

In this appendix we provide a self-contained review of basic definitions and properties of the proper orthogonal decomposition (POD) technique relevant to this work and discuss how the method can be applied to computer simulations in order to separate spatial and temporal behavior. Readers familiar with the technique can skip this section. The POD is a well-known technique for determining an optimal basis for the reconstruction of a data set.[23,24] It has been used in various disciplines that include fluid mechanics,[25–27] identification and control in chemical engineering,[28] oceanography,[29] and image processing.[30] Depending on the discipline, the POD is also known as Karhunen–Loève decomposition, principal components analysis, singular systems analysis, or singular value decomposition.

1. Theoretical aspects

Let us consider a sequence of numerical and/or experimental observations represented by scalar functions $u(\mathbf{x}, t_i)$, $i = 1 \ldots M$. Without loss of generality, the time-average of the sequence, defined by

$$\bar{u}(\mathbf{x}) = \langle u(\mathbf{x}, t_i) \rangle = \frac{1}{M} \sum_{i=1}^{M} u(\mathbf{x}, t_i), \tag{A1}$$

is assumed to be zero. The proper orthogonal decomposition extracts time-independent orthonormal basis functions, $\Phi_k(\mathbf{x})$, and time-dependent orthonormal amplitude coefficients, $a_k(t_i)$, such that the reconstruction

$$u(\mathbf{x}, t_i) = \sum_{k=1}^{M} a_k(t_i) \Phi_k(\mathbf{x}), \quad i = 1, \ldots, M \tag{A2}$$

is optimal in the sense that the average least squares truncation error

$$\varepsilon_m = \left\langle \left\| u(\mathbf{x}, t_i) - \sum_{k=1}^{m} a_k(t_i) \Phi_k(\mathbf{x}) \right\|^2 \right\rangle \tag{A3}$$

is minimized for any given number $m \leq M$ of basis functions over all possible sets of orthogonal functions. Here $\|\cdot\|$ is the L^2-norm, $\|f\|^2 = (f, f)$, where $(\cdot, \cdot)$ denotes the standard Euclidean inner product; $\langle \cdot \rangle$ denotes an average operation, usually over time; and the functions $\Phi_k(\mathbf{x})$ are called *empirical eigenfunctions, coherent structures*, or *POD modes*. In practice the state of a numerical model is only available at discrete spatial grid points, so that the observations that form the data set are vectors rather than continuous functions. In other words, $D = (x_1, x_2, \ldots, x_N)$, where x_j is the jth grid point and $u(\mathbf{x}, t_i)$ is the vector $\mathbf{u}_i = [u(x_1, t_i), u(x_2, t_i), \ldots, u(x_N, t_i)]^T$. The data set can be obtained from numerical simulation, experimental investigation or a combination of the numerical and experimental results. More importantly, it can be shown that the eigenfunctions Φ_k are the eigenvectors of the tensor product matrix

$$S(\mathbf{x},\mathbf{y}) = \frac{1}{M}\sum_{i=1}^{M} \mathbf{u}_i\mathbf{u}_i^T. \tag{A4}$$

2. Computational implementation: Method of snapshots

A popular technique for finding the eigenvectors of (A4) is the *method of snapshots* developed by Sirovich.[31–33] It was introduced as an efficient method when the resolution of the spatial domain (N) is higher than the number of observations (M). The method of snapshots is based on the fact that the data vectors, $\mathbf{u}_i$, and the eigenvectors Φ_k, span the same linear space.[26,31] This implies that the eigenvectors can be written as a linear combination of the data vectors

$$\Phi_k = \sum_{i=1}^{M} v_i^k \mathbf{u}_i, \quad k=1\ldots M. \tag{A5}$$

After substitution in the eigenvalue problem, $S(\mathbf{x},\mathbf{y})\Phi(\mathbf{y}) = \lambda\Phi(\mathbf{x})$, the coefficients v_i^k are obtained from the solution of

$$C\mathbf{v} = \lambda\mathbf{v}, \tag{A6}$$

where $\mathbf{v^k} = (v_1^k,\ldots,v_M^k)$ is the kth eigenvector of (A6), and C is a symmetric $M\times M$ matrix defined by $[c_{ij}] = (1/M) \times (\mathbf{u}_i,\mathbf{u}_j)$. Here $(\cdot,\cdot)$ denotes the standard vector inner product, $(\mathbf{u}_i,\mathbf{u}_j) = u(x_1,t_i)u(x_1,t_j) + \cdots + u(x_N,t_i)u(x_N,t_j)$. In this way the eigenvectors of the $N\times N$ matrix S (A4) can be found by computing the eigenvectors of an $M\times M$ matrix C (A6), a preferable task if $N\gg M$. The results presented in Sec. IV were obtained with an implementation of the method of snapshots.

3. Properties of the POD decomposition

Since the kernel is Hermitian, $S(\mathbf{x},\mathbf{y}) = S^*(\mathbf{y},\mathbf{x})$, according to the Riesz theorem,[34] it admits a diagonal decomposition of the form

$$S(\mathbf{x},\mathbf{y}) = \sum_{k=1}^{N} \lambda_k\Phi_k(\mathbf{x})\Phi_k^*(\mathbf{y}). \tag{A7}$$

This fact is particularly useful when finding the POD modes analytically. They can be read off from the diagonal decomposition (A7). Then the temporal coefficients, $a_k(t_i)$, are calculated by projecting the data set on each of the eigenfunctions

$$a_k(t_i) = (u(\mathbf{x},t_i),\Phi_k(\mathbf{x})), \quad i=1,\ldots,M. \tag{A8}$$

It can be shown that both temporal coefficients and eigenfunctions are uncorrelated in time and space, respectively.[26,31–33] In addition, the POD modes $\{\Phi_k(\mathbf{x})\}$ and the corresponding temporal coefficients, $\{a_k(t_i)\}$, satisfy the following orthogonality properties:

(i) $\Phi_j^*(\mathbf{x})\Phi_k(\mathbf{x}) = \delta_{jk}$,

(ii) $\langle a_j(t_i)a_k^*(t_i)\rangle = \delta_{jk}\lambda_j$,

where δ_{jk} represents the Kronecker delta function.

Property (ii) is obtained when the terms in the diagonal decomposition (A7) are compared with the expression

$S(\mathbf{x},\mathbf{y}) = \Sigma\langle a_j(t_i)a_k^*(t_i)\rangle\Phi_j(\mathbf{x})\Phi_k^*(\mathbf{y})$. The nonnegative and self-adjoint properties of $S(\mathbf{x},\mathbf{y})$ imply that all eigenvalues are nonnegative and can be ordered accordingly: $\lambda_1 \geqslant \lambda_2\ldots \geqslant\ldots\geqslant 0$. Statistically speaking, λ_k represents the variance of the data set in the direction of the corresponding POD mode, $\Phi_k(\mathbf{x})$. In physical terms, if u represents a component of a velocity field, then λ_k measures the amount of kinetic energy captured by the respective POD mode, $\Phi_k(\mathbf{x})$. In this sense, the energy measures the contribution of each mode to the overall dynamics.

The total energy captured in a proper orthogonal decomposition of a numerical or experimental data set is defined as the sum of all eigenvalues

$$E = \sum_{k=1}^{M} \lambda_k. \tag{A9}$$

The relative energy captured by the kth *mode*, E_k, is defined by

$$E_k = \frac{\lambda_k}{\sum_{j=1}^{M} \lambda_j}. \tag{A10}$$

Note that the cumulative sum of relative energies, ΣE_k, approaches one as the number of modes in the reconstruction increases to M. The relative phase-angle between two POD-time coefficients is defined by

$$\theta_{ij} = a\tan\left(\frac{a_i}{a_j}\right). \tag{A11}$$

[1] M. Gorman, M. el Hamdi, and K. Robbins, "Experimental observations of ordered states of cellular flames," Combust. Sci. Technol. **98**, 37–45 (1994).

[2] A. Turing, "The chemical basis of morphogenesis," Philos. Trans. R. Soc. London, Ser. B **237**, 37–72 (1952)

[3] M. Gorman, M. el Hamdi, and K. Robbins, "Rotating and modulated rotating states of cellular flames," Combust. Sci. Technol. **98**, 25–35 (1994).

[4] A. Palacios, G. Gunaratne, and M. Gorman, "Modal decomposition of hopping motion in cellular flame patterns," Chaos **9**, 755–767 (1999).

[5] M. Gorman, M. el Hamdi, and K. Robbins, "Hopping motion in ordered states of cellular flames," Combust. Sci. Technol. **98**, 71–78 (1994).

[6] J. Buckmaster, *The Mathematics of Combustion* (SIAM, Philadelphia, 1985).

[7] A. Bayliss, B. Matkowsky, and H. Riecke, "Structure and dynamics of modulated traveling waves in cellular flames," SIAM (Soc. Ind. Appl. Math.) J. Appl. Math. **74**, 1–23 (1994).

[8] P. Blomgren, S. Gasner, and A. Palacios, "A stable second-order scheme for integrating the Kuramoto–Sivashinky equation in polar coordinates," Phys. Rev. E. submitted.

[9] Y. Kuramoto, "Diffusion induced chaos in reaction systems," Suppl. Prog. Theor. Phys. **64**, 346–367 (1978).

[10] G. Sivashinsky, "Nonlinear analysis of hydrodynamic instability in laminar flames. Part I. Derivation of basic equations," Acta Astraunica **4**, 1177–1206 (1977).

[11] M. Gorman, C. Hamill, M. el Hamdi, and K. Robbins, "Four types of chaotic dynamics in cellular flames," Combust. Sci. Technol. **98**, 79–93 (1994).

[12] A. Palacios, G. Gunaratne, M. Gorman, and K. Robbins. "Cellular pattern formation in circular domains," Chaos **7**, 463–475 (1997).

[13] B. J. Matkowsky, L. J. Putnick, and G. I. Sivashinsky, "A nonlinear theory of cellular flames," SIAM (Soc. Ind. Appl. Math.) J. Appl. Math. **38**, 489–504 (1980).

[14] D. Zhang, G. Wei, D. Kouri, D. Hoffmann, A. Palacios, M. Gorman, and G. Gunaratne, "Integrating the Kuramoto–Sivashinsky equation in a circular domain," Phys. Rev. E **60**, 3353–3360 (1999).

[15] A. M. Frishman, D. K. Hoffman, R. J. Rakauskas, and D. J. Kouri, "Distributed approximating functional approach to fitting and predicting potential surfaces atom–atom potentials," Chem. Phys. Lett. **151**, 62–70 (1996).

[16] D. Hoffman, M. Arnold, and D. Kouri, "Properties of the optimum distributed approximating function class propagator for discretized and continuous wave packet propagations," J. Phys. Chem. **96**, 6539–6545 (1992).

[17] D. Hoffman, T. Marchioro II, M. Arnold, Y. Huang, W. Zhu, and D. Kouri, "Variational derivation and extensions of distributed approximating functionals," J. Math. Chem. **20**, 117–140 (1996).

[18] J. C. Strikwerda, *Finite Difference Schemes and Partial Differential Equations*, 2nd ed., (SIAM, Philadelphia, 2004) (first edition is out of print).

[19] A. Palacios, G. Gunaratne, M. Gorman, and K. Robbins, "A Karhunen–Loève analysis of spatiotemporal flame patterns," Phys. Rev. E **57**, 5958–5971 (1998).

[20] M. Dellnitz, M. Golubitsky, and M. Nicol, "Symmetry of attractors and the Karhunen–Loève decomposition," in *Trends and Perspectives in Applied Mathematics*, edited by L. Sirovich (Springer-Verlag, New York, 1994), Vol. 100, pp. 73–108.

[21] G. Gunaratne, M. el Hamdi, M. Gorman, and K. Robbins, "Asymmetric cells and rotating rings in cellular flames," Mod. Phys. Lett. B **10**, 1379–1388 (1996).

[22] A. Palacios, "Identification of modulated rotating waves in pattern-forming systems with $\mathbf{O}(2)$ symmetry," Discrete Contin. Dyn. Syst., Ser. B **2**, 129–147 (2002).

[23] K. Karhunen, "Zur spektraltheorie stochasticher prozesse," Ann. Acad. Sci. Fenn., Ser. A **37**, 3–76 (1946).

[24] M. Loève, *Probability Theory* (Van Nostrand, New York, 1955).

[25] G. Berkooz, P. Holmes, and J. L. Lumley, "The proper orthogonal decomposition in the analysis of turbulent flows," Annu. Rev. Fluid Mech. **25**, 539–575 (1993).

[26] P. Holmes, J. L. Lumley, and G. Berkooz, *Turbulence, Coherent Structures, Dynamical Systems and Symmetry* (Cambridge University Press, Cambridge, 1996).

[27] J. L. Lumley, "The structure of inhomogeneous turbulent flows," in *Atmospheric Turbulence and Radio Wave Propagation*, edited by A. M. Yaglom and V. I. Tatarski (Nauka, Moscow, 1967), pp. 166–178.

[28] M. D. Graham, S. L. Lane, and D. Luss, "Proper orthogonal decomposition analysis of spatiotemporal temperature patterns," J. Phys. Chem. **97**, 889–894 (1993).

[29] R. Preisendorfer, *Principal Component Analysis in Meteorology and Oceanography*, edited by C. Mobley (Elsevier, Amsterdam, 1988).

[30] K. W. Pratt, *Digital Image Processing*, 2nd ed. (Wiley, New York, 1991).

[31] L. Sirovich, "Turbulence and the dynamics of coherent structures, Part I: Coherent structures," Q. Appl. Math. **45**, 561–590 (1987).

[32] L. Sirovich, "Turbulence and the dynamics of coherent structures, Part II: Symmetries and transformations," Q. Appl. Math. **45**, 573–582 (1987).

[33] L. Sirovich, "Turbulence and the dynamics of coherent structures, Part III: Dynamics and scaling," Q. Appl. Math. **45**, 583–590 (1987).

[34] F. Riesz and B. Sz.-Nagy, *Functional Analysis* (Dover, New York, 1990).